

Sparse multiway decomposition for analysis and modeling of diffusion imaging and tractography

CESAR F. CAIAFA*

Instituto Argentino de Radioastronomía (IAR) - CONICET, CCT-La Plata,
Buenos Aires, ARGENTINA.
ccaiafa@gmail.com

FRANCO PESTILLI

Dept. of Psychological and Brain Sciences, Programs in Neuroscience and Cognitive Science,
Indiana Network Science Institute, Indiana University, Bloomington, IN, USA.
franpest@indiana.edu

Abstract

The number of neuroimaging data sets publicly available is growing at fast rate. The increase in availability and resolution of neuroimaging data requires modern approaches to signal processing for data analysis and results validation. We introduce the application of sparse multiway decomposition methods (Caiafa and Cichocki, 2012) to linearized neuroimaging models. We show that decomposed models are more compact but as accurate as full models and can be successfully used for fast data analysis. We focus as example on a recent model for the evaluation of white matter connectomes (Pestilli et al, 2014). We show that the multiway decomposed model achieves accuracy comparable to the full model, while requiring only a small fraction of the memory and compute time. The approach has implications for a majority of neuroimaging methods using linear approximations to measured signals.

Keywords. Brain anatomy, Big data, Brain mapping, Brain networks, Connectomics, High-performance computing, Individualized medicine, Myeline, Personalized medicine, Precision medicine, Tensor decomposition.

I. INTRODUCTION

NEUROSCIENCE is transforming. Investigators have recently started sharing brain data collected on large human populations (Scott et al, 2011; Van Essen and Ugurbil, 2012; Van Essen et al, 2013). The modern era of data sharing has the potential to promote scientific replicability of results and advance our understanding of brain function. Shared data can be accessed by different research groups and analytic tools can be tested and applied to the very same data in attempt to extend and replicate scientific results (Pestilli, 2015; Zuo et al, 2014). This fundamental shift of modern neuroscience will allow separating the wheat from the chaff. This paradigm shift is changing the landscape of brain imaging and motivating

investigators to implement new methods for data storage, analysis and sharing (Pestilli, 2015).

Hereafter, we show that modern neuroimaging can benefit from recent developments in signal processing (Caiafa and Cichocki, 2012; Cichocki et al, 2015) to address the new challenges raised by the most recent growth in data size, resolution and neuroscience models complexity. Standard signal processing methods in neuroimaging are based on classical Linear Algebra and use mathematical objects such as one dimensional vectors (1D) and two dimensional matrices (2D). Multiway approaches exploit the properties of arrays of higher order; arrays with three or more dimensions. Multiway arrays, also referred to as hypermatrices or tensors, are the generalization

*Also with Facultad de Ingeniería, University of Buenos Aires, ARGENTINA.

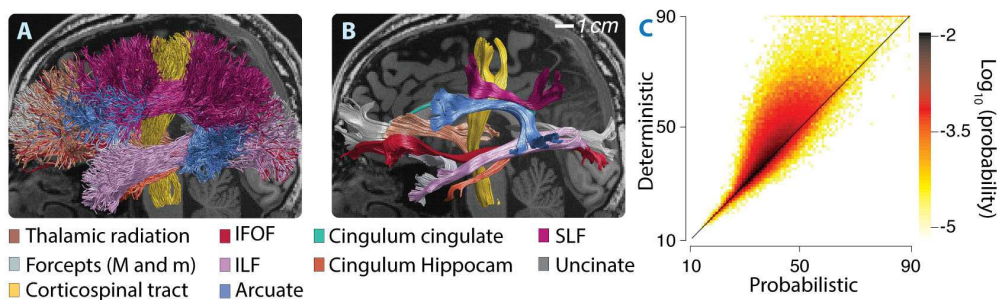


Figure 1: *Tractography comparison and evaluation. A. Ten major human white matter tracts generated using probabilistic tractography. B. Ten major human white matter tracts generated using deterministic tractography. C. Comparison of r.m.s. errors in predicting the diffusion signal of probabilistic and deterministic connectomes.*

of vectors and matrices to higher number of dimensions (ND). Multiway arrays have two primary advantages when applied to neuroimaging data compared to classical linear algebra approaches. First, neuroimaging data are multidimensional in nature and their structure is preserved by multiway arrays, which in turns allows for straightforward data addressing. Second, they provide convenient and compact representations of neuroimaging models that allows substantial reduction in memory consumption (Caiafa and Cichocki, 2013; Cichocki et al, 2015; Mørup, 2011). Below we briefly introduce basic concepts for multyway array decomposition and show one example application of the methods to modeling diffusion imaging and tractography (Pestilli et al, 2014).

dMRI data in combination with fiber tracking allows measuring the anatomy and tissue properties of the human white-matter in living brains (Yeatman et al, 2012; Yendiki et al, 2011; Zhang et al, 2010). By measuring living brains this technology allows correlating the properties of the white matter tissue and structure with human behavior, cognition as well as development and aging in health and disease (Samanez-Larkin and Knutson, 2015; Thomason and Thompson, 2011). dMRI and tractography generate estimates of white matter tracts and connections, such estimates need methods for routine evaluation and validation (Catani et al, 2012; Jones et al, 2013; Sporns et al, 2005). For example, it is established that different tractography methods can generate different estimates of the shape

of the white matter anatomy (Fig. 1A and B).

Recently we developed a method called LiFE, Linear Fascicle Evaluation (Pestilli et al, 2014). LiFE is an approach to statistical validation of in vivo connectomes that can be applied to individual brains. To validate connectomes in each brain, LiFE requires as input a set of candidate white-matter fascicles generated using available tractography algorithms (Cook et al, 2006; Jiang et al, 2006; Tournier et al, 2012). The candidate fascicles are used to generate a prediction of the anisotropic diffusion signal measured within the white matter volume using dMRI. The error (root mean squared error, r.m.s.) in predicting the diffusion signal is computed using cross-validation and used to establish the accuracy of a tractography solution. For example, Fig. 1C shows a comparison of the cross-validated r.m.s. error of two tractography methods in the same brain (the models shown in Fig. 1A and 1B). The result demonstrate that in a majority of the white matter the model in Fig. 1A has lower r.m.s. error in predicting the diffusion signal.

LiFE predicts the demeaned dMRI data by finding the linear combination of the diffusion prediction contributed by all individual fascicles within a connectome.

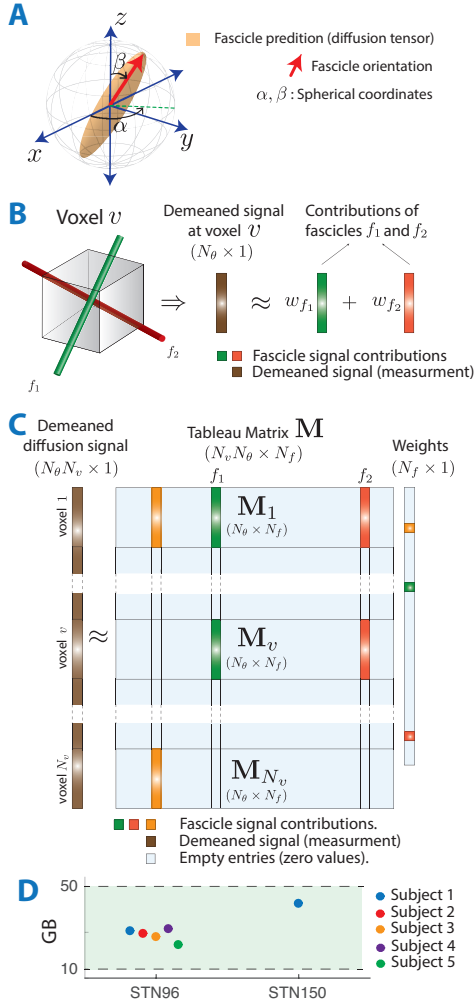


Figure 2: The linear fascicle evaluation method (LiFE). **A.** Idealized diffusion prediction model for the fascicles in a voxel. The fiber-predicted diffusion signal in a voxel is modeled by the Steijkal-Tanner equation (orange surface; Basser and Pierpaoli (2011); Stejskal and Tanner (1965)), evaluated in the direction of each fascicle in the voxel (red arrow). **B.** The diffusion prediction in a voxel with multiple fascicles is computed as a linear combination of the prediction of each individual fascicle (Eq. 5). The demeaned diffusion signal (brown) is predicted as the weighted sum of the predictions from all fascicles (green and red) in the voxel. **C.** Global linear model. The demeaned measured diffusion signal across all white-matter voxels is organized in a long 1D vector (\mathbf{y}). The signal prediction from all fascicle across the full white-matter volume is organized into a large 2D block-sparse matrix \mathbf{M} . Weights are assigned to each fascicle using an optimization procedure, fascicle weights are organized into a 1D vector (\mathbf{w}). Notations, N_θ represents the number of diffusion directions, N_v the number of voxels, and N_f the number of fascicles). **D.** LiFE storage measurements. The size of the LiFE Model (2D matrix \mathbf{M} in Panel C) measured in GB in several brains and data sets. Matrices built using double floating-point precision.

The fundamental problem solved by LiFE is to allow computing an error measure that can be used for a variety of tasks in evaluating individual connectomes properties generated with virtually any tractography method (Gomez et al, 2015; Pestilli et al, 2014; Takemura et al, 2015; Yeatman et al, 2014). One consequence of formulating the LiFE model as a system of linear equations is the size of the 2D matrix representing the model (see Fig. 2C and Eq. 8). The computational demands of the LiFE method represented as 2D matrix are substantial. Given an approximate human white-matter volume of 500ml, the spatial and directional resolution of modern dMRI measurements and a reasonable number of fascicles in a connectome, the size of the LiFE model can be as large as about 50GB (see Fig. 2D).

Hereafter, we introduce a multiway decomposition method that reduces the size of the LiFE model by over 97%. The new multiway approach maintains memory consumption under 1GB per brain. The approach can be applied to any linearized model for global tractography, tractography evaluation and microstructure estimation. Below, we (1) describe the mathematics of the sparse multiway decomposition, (2) show that memory consumption is quasi-constant as function of connectome size when using the decomposition and (3) replicate major results of the original LiFE work using the new approach and several datasets (Pestilli et al, 2014). We provide open source software implementing the LiFE model at github.com/brain-life/life and francopestilli.github.io/life. Scripts and data used to generate the results in the present articles can be found at these repositories.

II. MATERIALS AND METHODS

I. Diffusion-weighted MRI acquisition

Diffusion-weighted Magnetic Resonance Imaging data (dMRI) were collected in five males subjects (age 37-39) at the Stanford Center for Cognitive and Neurobiological Imaging using a 3T Gen-

eral Electric Discovery 750 (General Electric Healthcare) equipped with a 32-channel head coil (Nova Medical). This dataset is published (Pestilli et al, 2014; Rokem et al, 2015) and publicly available at <http://purl.stanford.edu/rt034xr8593> and <http://purl.stanford.edu/ng782rw8378>. Data collection procedures were approved by the Stanford University Institutional Review Board. Written consent was collected from each participant.

Stanford 96 diffusion directions data set (STN96): two diffusion-weighted with whole-brain volume coverage were acquired in five individuals within a single scan session using a dual-spin echo diffusion-weighted sequence. Water-proton diffusion was measured using 96 directions chosen using the electrostatic repulsion algorithm (Jones et al, 1999). Diffusion-weighting gradient strength was set to $2,000\text{s/mm}^2$ ($TE = 96.8\text{ms}$). Data were acquired at 1.5mm^3 isotropic spatial resolution. Individual data sets were acquired twice and averaged in k-space ($NEX = 2$). Ten non-diffusion-weighted ($b = 0$) images were acquired at the beginning of each scan.

Stanford 150 diffusion directions data set (STN150): for one subject two dMRI data sets were also acquired in a single session using 150 directions, 2mm^3 isotropic spatial resolution and b values of $2,000\text{s/mm}^2$ ($TE = 83.1, 93.6, \text{ and } 106.9\text{ms}$).

MRI images for STN96 and STN150 were corrected for spatial distortions due to B0 field inhomogeneity. To do so, B0 magnetic field maps were collected with the same slice prescription as the dMRI data using a 16-shot, gradient-echo spiral-trajectory pulse sequence. Two volumes were acquired before and after the dMRI scan ($TE = 9.091\text{ms}$ and 11.363ms respectively), the phase difference between the volumes was used as an estimate of the magnetic field.

Subjects' motion was corrected using a rigid-body alignment algorithm (Friston et al, 2004). Diffusion gradients were adjusted to account for the rotation applied to the measurements during motion correction. The dual-spin echo sequence we used does not require eddy current correction because it has a relatively

long delay between the RF excitation pulse and image acquisition. This allows for sufficient time for the eddy currents to dephase. Processing software is available at <https://github.com/vistalab/vistasoft>.

II. Anatomical MRI acquisition and tissue segmentation

The white/gray matter border was defined on the average of two 0.7-mm³ T1-weighted FSPGR images acquired in the same scan session. Tissue segmentation was performed using an automated procedure (FreeSurfer Fischl (2012)) and refined manually (<http://www.itksnap.org/pmwiki/pmwiki.php>).

III. Whole-brain connectomes generation and visualization

Fiber tracking was performed using the MRtrix 0.2 toolbox (Tournier et al, 2012). White-matter tissue was identified from the cortical segmentation performed on the T1-weighted images and resampled at the resolution of the dMRI data. Only white-matter voxels were used to seed fiber tracking. We used two tracking methods: (i) tensor-based deterministic tractography (Basser et al, 2000; Lazar et al, 2003; Tournier et al, 2012) and (ii) CSD-based probabilistic tracking (Behrens et al, 2003a; Parker et al, 2003; Tournier et al, 2012) with a maximum harmonic order of 10 ($L_{max} = 10$, step size: 0.2mm ; minimum radius of curvature, 1mm ; maximum length, 200mm ; minimum length, 10mm ; fibers orientation distribution function (f_{ODF}) amplitude cutoff, was set to 0.1).

We created candidate whole-brain connectomes with 500,000 fascicles in each individual brain (five), data set (two) and tractography method (two). Analysis were performed independently for each brain. Figures of tracts and brain images were generated using the Matlab Brain Anatomy toolbox: <https://github.com/francopestilli/mba>.

IV. Brief introduction to modeling magnetic resonance diffusion signals from living human brain tissue

The brain tissue comprises different cell types (e.g., neurons, astrocytes and oligodendrocytes). dMRI measures signals that depends on the combination of all cellular components within the brain tissue. The dMRI measurements are generally modeled as the linear combination of two primary components. One component describes the directional diffusion signal and is presumably related primarily to the direction of the neuronal axons wrapped in myelin sheaths (white matter). This signal is often referred to as *anisotropic diffusion*. The other component describes *isotropic diffusion* (non-directional) and is presumably related to the combination of signals originating from the rest of the cellular bodies within the brain tissue. Below we describe the simplest, fundamental equations used to model the measured dMRI signal in relation to the brain tissue components.

dMRI measures the diffusion signal with and without diffusion sensitization. The measured signal results from the combination of diffusion gradient strength, duration and depends on the interval between two applied gradient pulses. Below we denote the strength of sensitization with b and the vectors of measured diffusion directions (directions along which the diffusion-sensitization gradients are applied) using the unit-norm vector $\boldsymbol{\theta} \in \mathbb{R}^3$.

For a given sensitization strength b and diffusion directions $\boldsymbol{\theta}$, the diffusion signal measured at each location within a brain (voxel v) can be computed using the following equation (Behrens et al, 2003b; Frank, 2002):

$$S(\boldsymbol{\theta}, v) \approx \mathbf{w}_0 S_0(v) e^{-A_0} + \sum_{f \in v} \mathbf{w}_f S_0(v) e^{-b \boldsymbol{\theta}^T \mathbf{Q}_f \boldsymbol{\theta}}, \quad (1)$$

where f is the index of the candidate white-matter fascicles within the voxel, $S_0(v)$ is the non diffusion-weighted signal in voxel v and A_0 is the isotropic apparent diffusion (diffusion in all directions). The value $\boldsymbol{\theta}^T \mathbf{Q}_f \boldsymbol{\theta} > 0$ gives us the apparent diffusion at direction $\boldsymbol{\theta}$

generated by fascicle f . $\mathbf{Q}_f \in \mathbb{R}^{3 \times 3}$ is a symmetric and positive-definite matrix called tensor (Basser et al, 1994). The tensor allows a compact representation of the diffusion signal measured with dMRI. For example, \mathbf{Q}_f in the exponent of Eq. 1 can be replaced with the following simple tensor model:

$$\mathbf{Q}_f = [\mathbf{u}_1 \quad \mathbf{u}_2 \quad \mathbf{u}_3] \begin{bmatrix} s_a & 0 & 0 \\ 0 & s_{r_1} & 0 \\ 0 & 0 & s_{r_2} \end{bmatrix} \begin{bmatrix} \mathbf{u}_1 \\ \mathbf{u}_2 \\ \mathbf{u}_3 \end{bmatrix}, \quad (2)$$

where $\mathbf{u}_n \in \mathbb{R}^{3 \times 1}$ are the unit-norm orthogonal vectors that correspond to the semi-axes of the diffusion tensor ellipsoid, and s_a, s_{r_1}, s_{r_2} define the axial and radial diffusivity of the tensor, respectively. In the simplest version of the fascicle model, $s_a = 1$ and $s_{r_1} = s_{r_2} = 0$, which means that diffusion is restricted to the main axis direction (Behrens et al, 2003b; Pestilli et al, 2014).

V. Brief introduction to multiway arrays

Multiway arrays generalize vectors (1D array) and matrices (2D array) to arrays of higher dimensions, three or more. Such arrays can be used to perform multidimensional factor analysis and decomposition and are of interest to many scientific disciplines (Cichocki et al, 2015; Kolda and Bader, 2009). Below we introduce a few basic concepts and notation helpful in discussing multiway arrays and their decomposition. We refer the reader to Table 1 for a summary of basic notations and definitions.

Multiway arrays. Vectors (1D arrays) and matrices (2D arrays) are denoted below using boldface lower- and upper-case letters, respectively. For example $\mathbf{x} \in \mathbb{R}^I$ and $\mathbf{X} \in \mathbb{R}^{I \times J}$ represent a vector and a matrix, respectively. A multiway array, also called N -th order array, is the generalization of matrices to more than two dimensions and is denoted by an underlined boldface capital letter, e.g. $\underline{\mathbf{X}} \in \mathbb{R}^{I \times J \times K}$ is a 3-rd order array of real numbers. Elements (i, j, k) of a multiway array are referred to as x_{ijk} .

Array slices. Array slices are used to address a multiway array along a single dimension (a cut through a single dimension of the

array). Slices are obtained by fixing the index of one dimension of the multiway array while letting the other indices vary. For example, in a 3-rd order array $\underline{\mathbf{X}} \in \mathbb{R}^{I \times J \times K}$, we can identify horizontal (i), lateral (j) and frontal (k) slices by holding fixed the corresponding index of each array dimension (see Fig. 3A).

Unfolding arrays and mode- n vectors. Multiway arrays can be conveniently addressed in any dimension by means of mode- n vectors. Given a multiway array $\underline{\mathbf{X}} \in \mathbb{R}^{I \times J \times K}$, its mode- n vectors are obtained by holding all indices fixed except one, thus corresponding to columns ($n = 1$), rows ($n = 2$) and so on (see Fig. 3B). For example, a 3D multiway array can be converted into a matrix by rearranging its entries (unfolding). The mode- n unfolded matrix, denoted by $\mathbf{X}_{(n)} \in \mathbb{R}^{I_n \times \bar{I}_n}$, where $\bar{I}_n = \prod_{m \neq n} I_m$ and whose entry at row i_n and column $(i_1 - 1)I_2 \cdots I_{n-1}I_{n+1} \cdots I_N + \cdots + (i_{N-1} - 1)I_N + i_N$ is equal to $x_{i_1 i_2 \dots i_N}$. For example, mode-2 unfolding builds the matrix $\mathbf{X}_{(2)}$ where its columns are the mode-2 vectors of the multiway array and the rows are vectorized versions of the lateral slices, i.e. spanning dimensions with indices i and k (see Fig. 3C).

Multiway array by matrix product. Multiway arrays can be multiplied by matrices (2D arrays) only if the matrix and multiway array sizes match in the mode specified for the multiplication. This is a generalization of matrix multiplication. Given a multiway array $\underline{\mathbf{X}} \in \mathbb{R}^{I_1 \times I_2 \times \dots \times I_N}$ and a matrix $\mathbf{A} \in \mathbb{R}^{J \times I_n}$, the mode- n product

$$\underline{\mathbf{Y}} = \underline{\mathbf{X}} \times_n \mathbf{A} \in \mathbb{R}^{I_1 \times \dots \times I_{n-1} \times J \times I_{n+1} \times \dots \times I_N} \quad (3)$$

is defined by:

$$y_{i_1 \dots i_{n-1} j i_{n+1} \dots i_N} = \sum_{i_n=1}^{I_n} x_{i_1 \dots i_n \dots i_N} a_{j i_n}, \quad (4)$$

with $i_k = 1, 2, \dots, I_k$ ($k \neq n$) and $j = 1, 2, \dots, J$. It is noted that this operation involves the products of matrix \mathbf{A} by each one of the mode- n vectors of $\underline{\mathbf{X}}$. In Fig. 3B, the 3-rd order array by matrix product in mode-2 is illustrated, i.e. $\underline{\mathbf{Y}} = \underline{\mathbf{X}} \times_2 \mathbf{A}$. The size of the resulting array $\underline{\mathbf{Y}}$ is that of $\underline{\mathbf{X}}$ in mode-1 and -3 while the size of $\underline{\mathbf{Y}}$ in mode-2 is J , i.e. it is

equal to the number of rows in \mathbf{A} .

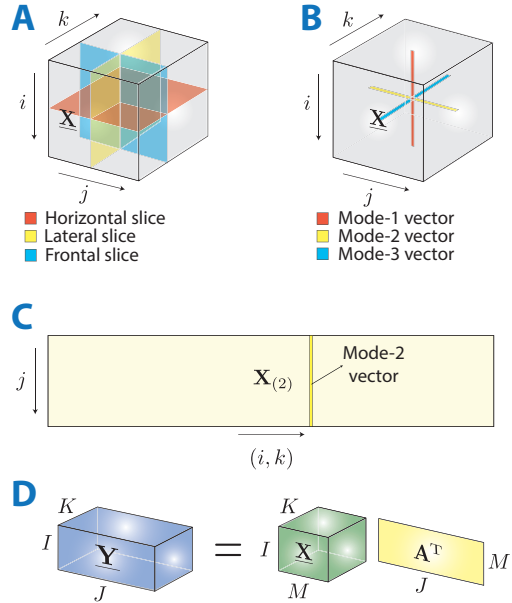


Figure 3: Multiway array decomposition basic notation and operations. **A.** Frontal, lateral and horizontal slices of an example multiway array. **B.** Examples of mode- n vectors. **C.** Illustration of the mode-2 unfolding matrix $\mathbf{X}_{(2)}$. **D.** Array-by-matrix product (example product in mode-2). See Table 1 for additional information about notation and mathematical definitions.

III. RESULTS

I. The Linear Fascicle Evaluation model

The Linear Fascicle Evaluation method (LiFE; Pestilli et al (2014)) allows evaluating the accuracy of connectomes generated using dMRI and any fiber tracking algorithm. The method evaluates the tractography solution by estimating the contribution to predicting the measured diffusion signal from all fascicles contained in a connectome (see Fig. 2A and B for examples of fascicles). The evaluation method focuses on the fascicles, for this reason it predicts the anisotropic diffusion signal; the demeaned diffusion signal (signal that is independent of isotropic diffusion, first term in the right hand of Eq. 1). The anisotropic signal within a voxel v is predicted by demeaning the signal prediction in

Table 1: Mathematical notation and definitions for multiway arrays and decomposition.

$\underline{\mathbf{X}}, \mathbf{A}, \mathbf{w}, b$	A tensor, a matrix, a vector and a scalar
$x_{i_1 i_2 \dots i_N}, a_{ij}, w_i$	Entries of a tensor, a matrix and a vector
$\underline{\mathbf{X}}(:, j, k), \underline{\mathbf{X}}(i, :, k), \underline{\mathbf{X}}(i, j, :)$	Mode-1, mode-2 and mode-3 vectors are obtained by fixing all but one index
$\underline{\mathbf{X}}(i, :, :), \underline{\mathbf{X}}(:, j, :), \underline{\mathbf{X}}(:, :, k)$	Horizontal, lateral and frontal slices are obtained by fixing all but two indices
$\mathbf{X}_{(n)} \in \mathbb{R}^{I_n \times I_1 I_2 \dots I_{n-1} I_{n+1} \dots I_N}$	Mode- n unfolding of multiway array $\underline{\mathbf{X}} \in \mathbb{R}^{I_1 \times I_2 \times \dots \times I_N}$ whose entry at row i_n and column $(i_1 - 1)I_2 \dots I_{n-1} I_{n+1} \dots I_N + \dots + (i_{n-1} - 1)I_N + i_N$ is equal to $x_{i_1 i_2 \dots i_N}$
$\underline{\mathbf{Y}} = \underline{\mathbf{X}} \times_n \mathbf{A} \in \mathbb{R}^{I_1 \times \dots \times I_{n-1} \times J \times I_{n+1} \times \dots \times I_N}$	Multiway array by matrix product (in mode- n) where $y_{i_1 \dots i_{n-1} i_{n+1} \dots i_N} = \sum_{j=1}^{I_n} x_{i_1 \dots i_n \dots i_N} a_{jin}$
$\underline{\mathbf{X}} \approx \underline{\mathbf{G}} \times_1 \mathbf{A}_1 \times_2 \mathbf{A}_2 \times_3 \mathbf{A}_3$	Tucker decomposition: a 3D multiway array $\underline{\mathbf{X}} \in \mathbb{R}^{I_1 \times I_2 \times I_3}$ is represented as the product of a core array $\underline{\mathbf{G}} \in \mathbb{R}^{R_1 \times R_2 \times R_3}$ by factor matrices $\mathbf{A}_n \in \mathbb{R}^{I_n \times R_n}$
$\mathbf{x} = \text{vec}(\underline{\mathbf{X}}) \in \mathbb{R}^{I_1 I_2 \dots I_N}$	Vectorization of multiway array $\underline{\mathbf{X}} \in \mathbb{R}^{I_1 \times I_2 \times \dots \times I_N}$ with the entry at position $i_1 + \sum_{k=2}^N [(i_k - 1)I_1 I_2 \dots I_{k-1}]$ equal to $x_{i_1 i_2 \dots i_N}$
$\mathbf{S}_0 = \text{diag}(S_0(1), S_0(2), \dots, S_0(N_v))$	Diagonal $N_v \times N_v$ matrix with $\mathbf{S}_0(v, v) = S_0(v)$

the following way:

$$S(\theta, v) - I_v \approx \sum_{f \in \mathcal{V}} w_f O_f(\theta), \quad (5)$$

where the mean I_v is defined as

$$I_v = \frac{1}{N_\theta} \sum_{\theta} S(\theta, v), \quad (6)$$

with N_θ being the number of sensitization directions and $O_f(\theta)$ is orientation distribution function specific to each fascicle, i.e. the anisotropic modulation of the diffusion signal around its mean and it is defined as follows:

$$O_f(\theta) = S_0(v) \left(e^{-b\theta^T \mathbf{Q}_f \theta} - \frac{1}{N_\theta} \sum_{\theta} e^{-b\theta^T \mathbf{Q}_f \theta} \right). \quad (7)$$

The left-side hand in Eq. 5, the demeaned signal, is the difference between the measured diffusion signal and the mean diffusion signal. The right-hand side of Eq. 5 is the prediction model. The LiFE model extends from the single voxel to all white-matter voxels in the following way:

$$\mathbf{y} \approx \mathbf{M}\mathbf{w}, \quad (8)$$

where $\mathbf{y} \in \mathbb{R}^{N_\theta N_v}$ is a vector containing the demeaned signal for all white-matter voxels v and across all diffusion directions θ , i.e. $y_i = S(\theta_i, v_i) - I_{v_i}$. The matrix $\mathbf{M} \in \mathbb{R}^{N_\theta N_v \times N_f}$ contains at column f the signal contribution $O_f(\theta)$ given by fascicle f at voxel v across all directions θ , i.e., $\mathbf{M}(i, f) =$

$O_f(\theta_i)$, and $\mathbf{w} \in \mathbb{R}^{N_f}$ contains the weights for each fascicle in the connectome. These weights are estimated by solving the following non-negative least-square constrained optimization problem:

$$\min_{\mathbf{w}} \left(\frac{1}{2} \|\mathbf{y} - \mathbf{M}\mathbf{w}\|^2 \right) \text{ subject to } w_f \geq 0, \forall f. \quad (9)$$

This formulation of the LiFE model requires generating a matrix \mathbf{M} (Fig. 2C) that is very large and block-sparse. \mathbf{M} is sparse because fascicles only cross a subset of all voxels. The matrix has $N_\theta N_v$ rows by N_f columns. Given an approximate human white-matter volume of 500 ml the number of voxels (N_v) can vary between 50,000 and 500,000 depending on the spatial resolution of the dMRI acquisition (normally between 4-1.25 mm³). Given that modern dMRI acquisition parameters measure between 30 and 300 diffusion directions (N_θ) and that whole-brain connectomes can contain as little as 100,000 but as much as 10,000,000 fascicles (columns of \mathbf{M}), the size of \mathbf{M} can vary between 10 and 100GB using standard double-precision floating-point format and sparse format.

Fig. 2D shows measurements of the size of \mathbf{M} in GB for five individual brains and two datasets. Such large memory requirements necessitate large-memory compute-systems nowadays available in major research institutions (e.g., <http://rt.uits.iu.edu/bigred2/>, <http://karst.uits.iu.edu>). Below we intro-

duce a novel approach that dramatically reduces the storage requirements of the LiFE model and makes LiFE suitable to run on standard desktop and notebook computers.

II. Multiway decomposition of the Linear Fascicle Evaluation model

Major contribution of the present work is a method to represent the LiFE model via Sparse Tucker Decomposition (STD; (Caiafa and Cichocki, 2012)). Before introducing the method, we briefly discuss the standard and sparse Tucker-decomposition methods (see also Methods 1).

Data compression by Tucker decomposition. Ledyard Tucker, a mathematician who specialized in statistics and psychometrics, was first in proposing a decomposition approach to multidimensional factorization problems (Tucker, 1966). The approach provides a generalization of the low-rank approximation for matrices to multiway arrays. Using the Tucker model, a 3-rd array $\underline{\mathbf{X}} \in \mathbb{R}^{I_1 \times I_2 \times I_3}$, is approximated by the following decomposition:

$$\underline{\mathbf{X}} \approx \underline{\mathbf{G}} \times_1 \mathbf{A}_1 \times_2 \mathbf{A}_2 \times_3 \mathbf{A}_3, \quad (10)$$

with a *core array* $\underline{\mathbf{G}} \in \mathbb{R}^{R_1 \times R_2 \times R_3}$ and *factor matrices* $\mathbf{A}_n \in \mathbb{R}^{I_n \times R_n}$. The decomposition is not guaranteed to provide a good approximation, but when it does it compresses data because it uses a core array that is much smaller than the original multiway array, i.e. $R_n \ll I_n$. Indeed, the Tucker model provides us with a powerful compression method. This is because, instead of storing the whole original multiway array, we can store core array and factors. In this case, Eq. 10 (Tucker, 1966) is called a *low-rank* Tucker model because $\underline{\mathbf{G}}$ is small compared to $\underline{\mathbf{X}}$ (see Fig. 4A).

A simple example can help us explain how compression is obtained with a standard low-rank Tucker model. Let consider a situation where $R = R_1 = R_2 = R_3$ and $I = I_1 = I_2 = I_3$. The low-rank Tucker decomposition of $\underline{\mathbf{X}}$ requires storing only $R^3 + 3IR$ values. Where R^3 is the number of entries of $\underline{\mathbf{G}}$ and I and R the dimensions of \mathbf{A}_1 , \mathbf{A}_2 and \mathbf{A}_3 . Instead, the full multiway array would require storing I^3 values, compression is no-

ticeable especially when $\underline{\mathbf{G}}$ is small meaning that $R \ll I$.

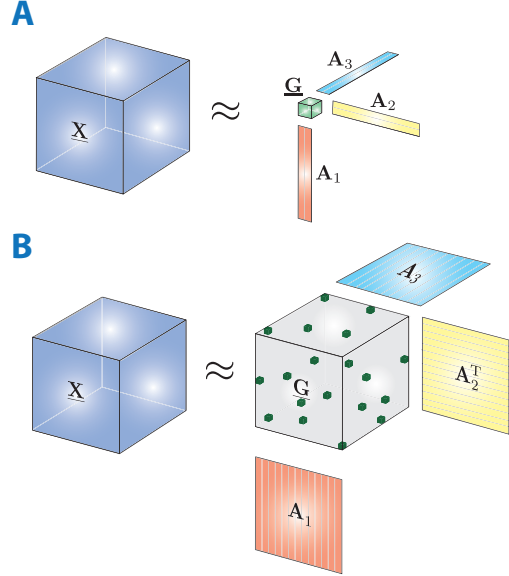


Figure 4: Classical and sparse Tucker decomposition. **A.** The classical Tucker decomposition (Tucker, 1966) allows representing a 3D multiway array $\underline{\mathbf{X}} \in \mathbb{R}^{I_1 \times I_2 \times I_3}$ as the product of core array (green) $\underline{\mathbf{G}} \in \mathbb{R}^{R_1 \times R_2 \times R_3}$ by factor matrices $\mathbf{A}_n \in \mathbb{R}^{I_n \times R_n}$ (red, yellow and blue). Data compression is achieved by considering very small (dense) core arrays $\underline{\mathbf{G}}$, meaning that $R_n \ll I_n$. **B.** The sparse Tucker Decomposition (STD; Caiafa and Cichocki (2012)). The core array $\underline{\mathbf{G}}$ is large but sparse, not dense as in the classical Tucker model. Data compression is achieved because of the sparsity of the core array.

Data compression by sparse Tucker decomposition: If the core $\underline{\mathbf{G}}$ of a Tucker decomposition of a multiway array is sparse, compression can be achieved even when $\underline{\mathbf{G}}$ is very large (Caiafa and Cichocki, 2012). Consider a Tucker model with a large but sparse core array $\underline{\mathbf{G}} \in \mathbb{R}^{R_1 \times R_2 \times R_3}$, see Fig. 3E. Only some entries in $\underline{\mathbf{G}}$ are nonzero, i.e. $g_{i_m j_m k_m} \neq 0$ for $m = 1, 2, \dots, M$ where M is the number of nonzero entries. Storing $\underline{\mathbf{G}}$ all requires storing: (1) the non-zero coefficients, (2) their location in $\underline{\mathbf{G}}$, and (3) the factor matrices \mathbf{A}_n . This means that the storage cost (order) of the model is $4M + 3IR$ (assuming that $R = R_1 = R_2 = R_3$ and $I = I_1 = I_2 = I_3$). Hereafter, we refer to this model as Sparse Tucker Decomposition (STD). Compared to the classical low-rank Tucker model, STD can provide better compression ratios with rela-

tively low M , i.e., with very sparse core arrays $\underline{\mathbf{G}}$ (Caiafa and Cichocki, 2013).

Below we show how to apply the STD approach to the LiFE model. To do so we first explain how the diffusion signals within a voxel predicted by the LiFE model can be represented using dictionaries of precomputed diffusion prediction signals. After that we show how to extend the decomposition approach to the whole white matter volume.

II.1 Decomposing LiFE within a voxel using prediction dictionaries

The original LiFE model predicts anisotropic diffusion within a voxel, v , at each measured diffusion direction, θ , by using the orientation of the white matter fascicles intersecting the voxel (Fig. 2B; Pestilli et al (2014)). Fascicles are defined as a list of (x, y, z) spatial coordinates within the brain, the fascicle *nodes*. To generate the prediction, a demeaned tensor model is evaluated parallel to the orientation of each fascicle node (Eq. 7). Hereafter, we simplify the calculations by representing the signal prediction for any arbitrary fascicle-node orientation using a dictionary of diffusion prediction signals generated for a predefined set of orientations regularly sampled over a grid. This grid covers a plausible range of fascicles orientations on the unit-norm sphere (shown in Fig. 2A) given the resolution of the dMRI data (Fig. 5A).

We define the dictionary matrix $\mathbf{D} \in \mathbb{R}^{N_\theta \times N_a}$ (Fig. 5B) containing in its columns the demeaned canonical diffusion signals called *atoms* that can be used to approximate fascicles' contributions. More specifically, we define

$$\mathbf{D}(\theta, a) = e^{-b\theta^T \mathbf{Q}_a \theta} - \frac{1}{N_\theta} \sum_{\theta} e^{-b\theta^T \mathbf{Q}_a \theta}, \quad (11)$$

where \mathbf{Q}_a is the diffusion prediction associated to the atom a , i.e. with a single orientation in 3D space. Dictionary atoms are identified by discretizing each spherical coordinate α and β using a grid of values in the range $[0, \pi)$ (Fig. 5B). The parameter L indicates the number of discretization samples on the grid. For example, $L = 180$ indicates a grid resolution of $1^\circ \times 1^\circ$ with an approxi-

mate atom number $N_a \approx L^2$.

The dictionary $\mathbf{D} \in \mathbb{R}^{N_\theta \times N_a}$ allows predicting the matrix $\mathbf{M}_v \in \mathbb{R}^{N_\theta \times N_f}$, defined as a block of matrix \mathbf{M} corresponding to voxel v (see Fig. 5C), by decomposing it in the following way:

$$\mathbf{M}_v = S_0(v) \mathbf{D} \Phi_v, \quad (12)$$

where $\Phi_v \in \mathbb{R}^{N_a \times N_f}$ is a sparse matrix whose non-zero entries at column f indicates the dictionary atoms selected to predict the voxel signal, given the orientations of the fascicles in the voxel. In sum, instead of storing the individual contribution of each fascicle within a voxel, we store only the indices to the dictionary atoms, and avoid multiple versions of very similar signals. Below we extend the STD of LiFE from single voxels to the entire white matter volume. We show that for each data set used we can find a finite number of dictionary atoms that generate predictions as accurate as those obtained with the original LiFE model.

II.2 Extending the LiFE decomposition model across all voxels

The original LiFE model comprises a single very large block-sparse matrix (\mathbf{M} in Eq. 8). The matrix $\mathbf{M} \in \mathbb{R}^{N_\theta N_v \times N_f}$ can be converted into a multiway array by mapping the diffusion directions (θ), voxels (v) and fascicles (f), onto the dimensions of a 3D multiway array $\underline{\mathbf{M}} \in \mathbb{R}^{N_\theta \times N_v \times N_f}$. Representing \mathbf{M} as a 3D multiway array $\underline{\mathbf{M}}$ allows us using a Sparse Tucker decomposition approach and compress its size (Caiafa and Cichocki, 2012).

To fully exploit the Sparse Tucker Decomposition we consider both the LiFE model \mathbf{M} and its optimization problem, as defined in Eq. 8. This equation can be conveniently rewritten using multiway arrays in the following manner (see Fig. 6A):

$$\mathbf{Y} \approx \underline{\mathbf{M}} \times_3 \mathbf{w}^T, \quad (13)$$

where matrix $\mathbf{Y} \in \mathbb{R}^{N_\theta \times N_v}$ is the matrix version of vector \mathbf{y} , and $\underline{\mathbf{M}} \in \mathbb{R}^{N_\theta \times N_v \times N_f}$ is a 3-way array. The lateral slices of $\underline{\mathbf{M}}$ are defined by the matrices $\mathbf{M}_v \in \mathbb{R}^{N_\theta \times N_f}$ defined in Eq. 12, these represent matrices \mathbf{M}_v correspond-

(f) node (n) is identified in spherical coordinates (α, β) ; (2) nodes' orientation is mapped to the closest atom (a) in the dictionary (\mathbf{D}); (3) the entry in $\underline{\Phi}$ corresponding to each identified voxel, fascicle and atom is set to 1:

$$\underline{\Phi}(a, v, f) = 1, \quad (16)$$

The rest of the entries in $\underline{\Phi}$ are set to zero.

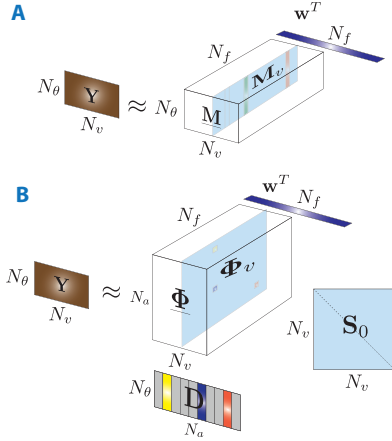


Figure 6: Sparse Tucker Decomposition of LiFE problem. **A.** Multiway version of the LiFE method $\mathbf{y} \approx \mathbf{M}\mathbf{w}$, Eq. 14. **B.** LiFE problem decomposition by Sparse Tucker method, Eq. 15.

IV. Optimizing the STD LiFE model

Building the STD LiFE model is the first of two steps in evaluating a brain connectome. The final step requires finding the non-negative weights that least-square fit the measured diffusion data. This is a convex problem that can be solved using a variety of Non-Negative Least Squares (NNLS) optimization algorithms (9). The original LiFE problem, was solved using a NNLS algorithm based on first-order methods (Kim et al, 2013). Hereafter, we show how to modify the optimization algorithm to exploit the STD LiFE model.

The optimization of the STD LiFE needs to be performed using its core array ($\underline{\Phi}$) and matrices (\mathbf{D} and \mathbf{S}_0 ; Eq. 14). The gradient of the original objective function for the LiFE model can be written as follows:

$$\nabla_{\mathbf{w}} \left(\frac{1}{2} \|\mathbf{y} - \mathbf{M}\mathbf{w}\|^2 \right) = \mathbf{M}^T \mathbf{M}\mathbf{w}, \quad (17)$$

where $\mathbf{M} \in \mathbb{R}^{N_\theta N_v \times N_f}$ is the original LiFE model, $\mathbf{w} \in \mathbb{R}_f^N$ the fascicle weights and $\mathbf{y} \in \mathbb{R}^{N_\theta N_v}$ the demeaned diffusion signal. Because the STD version does not explicitly store \mathbf{M} in the following section we describe how to perform two basic operations ($\mathbf{y} = \mathbf{M}\mathbf{w}$ and $\mathbf{w} = \mathbf{M}^T \mathbf{y}$) using the multiway decomposition to compute the optimization gradient. Appendix A reports pseudocode implementing the operations.

IV.1 Computing $\mathbf{y} = \mathbf{M}\mathbf{w}$

The product $\mathbf{M}\mathbf{w}$ can be computed in the following way using a 3D-array by vector product:

$$\mathbf{Y} = \underline{\mathbf{M}} \times_3 \mathbf{w}^T, \quad (18)$$

where the result is a matrix $\mathbf{Y} \in \mathbb{R}^{N_\theta \times N_v}$, a matrix version of the vector \mathbf{y} . Using the STD LiFE model (Eq. 14) the product is written as follows:

$$\mathbf{Y} = \underline{\Phi} \times_1 \mathbf{D} \times_2 \mathbf{S}_0 \times_3 \mathbf{w}^T. \quad (19)$$

IV.2 Computing $\mathbf{w} = \mathbf{M}^T \mathbf{y}$

The product $\mathbf{w} = \mathbf{M}^T \mathbf{y}$ can be computed using the STD LiFE model in the following way (Kolda and Bader, 2009):

$$\mathbf{w} = \mathbf{M}^T \mathbf{y} = \mathbf{M}_{(3)} \mathbf{y} = \underline{\Phi}_{(3)} (\mathbf{S}_0 \otimes \mathbf{D}^T) \mathbf{y}, \quad (20)$$

where \otimes is the Kronecker product. Eq. 20 equation can be written as follows:

$$\mathbf{w} = \underline{\Phi}_{(3)} \text{vec}(\mathbf{D}^T \mathbf{Y} \mathbf{S}_0), \quad (21)$$

where $\text{vec}()$ stands for the vectorization operation, i.e. to convert a matrix to a vector by stacking its columns in a long vector (Caiafa and Cichocki, 2012).

Because matrix $\underline{\Phi}_{(3)}$ is very sparse, we avoid computing the large and dense matrix $\mathbf{D}^T \mathbf{Y} \mathbf{S}_0$ and multiply only the non-zero entries in $\underline{\Phi}_{(3)}$. This allows maintaining efficient memory usage and limits the necessary number of CPU cycles.

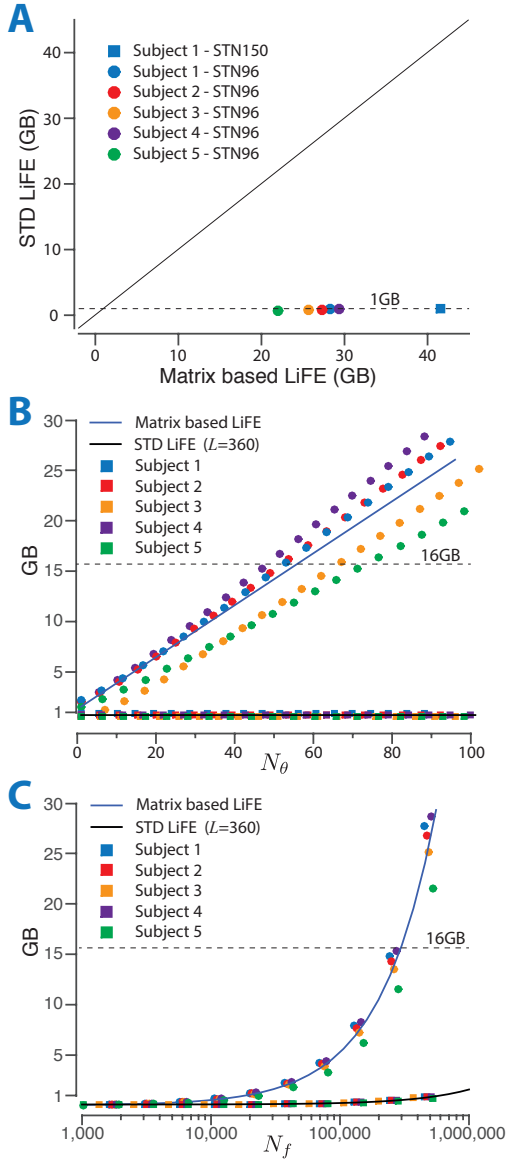


Figure 7: Reduction in memory usage using STD LiFE. **A.** The memory requirement of \mathbf{M} plotted against memory requirement of the STD model (Eq. 14, $L = 360$, STN96 data, probabilistic tractography, $L_{max} = 10$). **B.** Memory requirement for \mathbf{M} and STD (Eq. 14) as function of the number of measured diffusion directions (N_{θ} , $L = 360$, STN96 data, probabilistic tractography, $L_{max} = 10$). **C.** Memory requirement for \mathbf{M} and STD (Eq. 14) as function of the number of fascicles in the connectome (N_f , $L = 360$, STN96 data, probabilistic tractography, $L_{max} = 10$)

V. Model storage reduction

Fig. 7A compares memory usage by \mathbf{M} (Fig. 2C; Pestilli et al (2014)) and the STD LiFE model (Eq. 14). The storage requirements of

\mathbf{M} and the STD model can also be computed analytically. To do so we assume that all fascicles have the same number of nodes N_n and that there are no more than one node per fascicle, per voxel. Under these assumptions the amount of memory necessary to store each fascicle f is proportional to $N_\theta N_n$, thus the storage cost of \mathbf{M} is:

$$C(\mathbf{M}) = \mathcal{O}(N_n N_\theta N_f). \quad (22)$$

Conversely, storing fascicles in the STD model require $4N_n$ values only (i.e. the set of the non-zero coefficients and their locations within the core multi-way array $\underline{\Phi}$). Thus the amount of memory required by the STD model is:

$$C(\underline{\mathbf{M}}) = \mathcal{O}(4N_n N_f + N_\theta N_a), \quad (23)$$

where $N_\theta N_a$ is the storage associated with the dictionary matrix $\mathbf{D} \in \mathbb{R}^{N_\theta \times N_a}$. Please note that \mathbf{S}_0 is absorbed as $\underline{\Phi} = \underline{\Phi} \times_2 \mathbf{S}_0$ without affecting sparsity, i.e., with no effect on the storage. Storage reduction can be straightforwardly computed as follows:

$$s_{red} = 1 - \frac{4}{N_\theta} - \frac{N_a}{N_n N_f}. \quad (24)$$

Fig. 7B shows memory usage for the models in (Pestilli et al, 2014) and Eq. 14 as function of number of diffusion directions N_θ in the data. Given a fixed number of fascicles N_f and nodes N_n in a brain storage of \mathbf{M} grows linearly with the number of diffusion directions (N_{θ} ; see Eq. 22) much faster than the STD model (Eq. 23).

Fig. 7C shows memory usage for the models in (Pestilli et al, 2014) and Eq. 14 as function of the number of fascicles in a connectome (N_f). The storage of \mathbf{M} grows linearly with N_f and grows much faster than the STD model.

In sum, the STD model provides substantial reduction in memory requirements. The reduction in memory consumption achieved by the STD model becomes more important as the number of measured directions and fascicles in a connectome increase.

VI. Model accuracy

The STD model provides only an approximation of the original LiFE model. This is because of the discretization introduced by the dictionary (\mathbf{D} , see Fig. 5A). Fig. 8 shows that the STD model achieves accuracy similar to the original model. We compared the accuracy of the STD model in both, predicting the demeaned signal and estimating the weights of the original model.

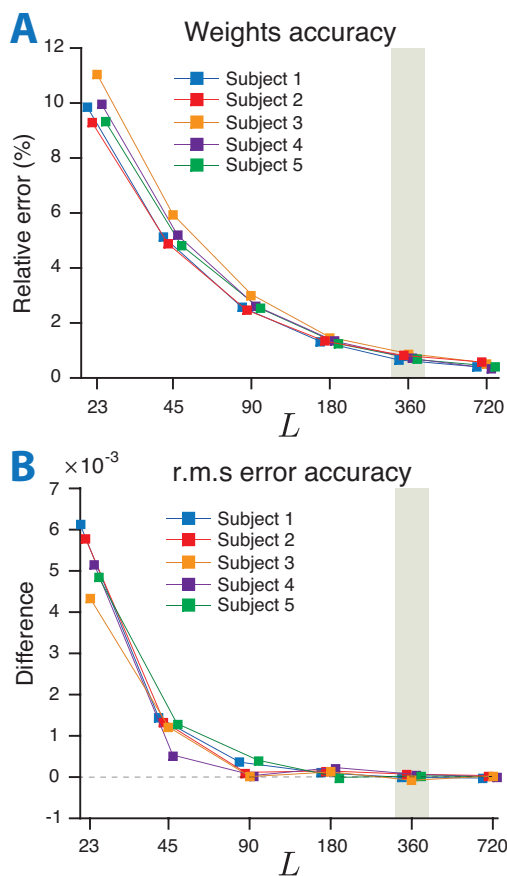


Figure 8: The STD model is as accurate as the original LiFE model. **A.** Difference in mean cross-validated r.m.s error for a range of discretization steps between the STD and original LiFE models. **B.** Relative error in estimating the fascicles weights between the STD and original LiFE model for a range of discretization steps (STN96 data, probabilistic tractography, $L_{max} = 10$).

Fig. 8A shows the difference between the r.m.s error of the STD and original LiFE model. We fit the STD model using different number of discretization steps of the spherical coordinates (5A). To do so, the number of discretization steps was varied

($L = 23, 45, 90, 180, 360$ and 720) and the difference in mean r.m.s. in predicting the demeaned diffusion signal across the whole white-matter volume was computed in reference to the mean r.m.s. of the original model. The mean r.m.s. used for comparison was cross-validated to an independent data set ((Pestilli et al, 2014)).

Fig. 8B shows the relative error of the STD model in estimating the weights assigned by the original LiFE model to each fascicle. We fit the STD model using different number of discretization steps of the spherical coordinates as in 8A. We computed the relative error in the estimated weights as $\|\mathbf{w}_0 - \mathbf{w}_1\|/\|\mathbf{w}_0\|$ where $\mathbf{w}_0, \mathbf{w}_1$ are the weights of the original and STD models, respectively. Results show that for the data sets tested, $L \geq 360$ allows achieving error below 1%.

VII. Reproduction of results from Pestilli et al (2014)

We demonstrated that a Sparse Tucker Decomposition model achieves similar accuracy to the original LiFE model and reduces storage requirements by 97%. Fig. 9 shows that the STD model replicates a major result of the original (Pestilli et al, 2014). The scatter plot shows the cross-validated r.m.s. in predicting the demeaned diffusion signal of a probabilistic and deterministic tractography connectome. Results show that the STD model replicates the findings of Pestilli et al (2014) demonstrating a larger r.m.s. for the deterministic tractography connectome in a majority of the white matter volume (see Fig. 1C for the same plot computed using the original LiFE model).

VIII. Open source LiFE software and reproducibility of results.

The Matlab implementation of LiFE software using the new STD model is provided at github.com/brain-life/life and francopestilli.github.io/life. The Matlab implementation uses the Matlab Tensor Toolbox (Bader et al, 2012) and mex files compiled for Mac OSX and 64-bit Linux distributions. The software has been tested

to run on a standard Notebook computers with less than 8GB of RAM. Processing a whole brain connectome with 500,000 fascicles of the STN150 dataset using a single CPU thread (Notebook computer, 2.2GHz Intel Core i7 processor and 8GB RAM) requires about 5 hours ($L = 360$).

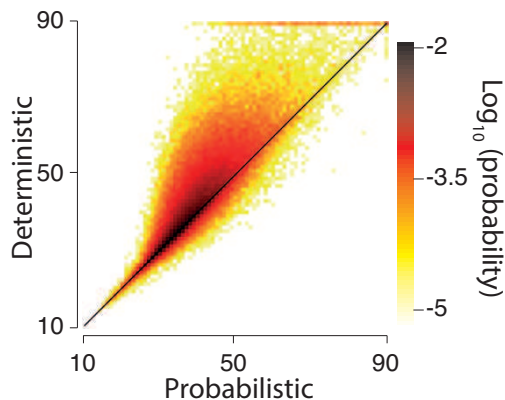


Figure 9: The STD model replicates major results of (Pestilli et al, 2014). The scatter plot shows the r.m.s. errors in predicting the demeaned diffusion signal of two tractography models. The r.m.s. error of a probabilistic connectome is plotted against that of a deterministic connectome. R.m.s. was computed using a single subjects from the STN96 data set using CSD-based probabilistic tractography ($L_{max} = 10$) and tensor-based deterministic tractography and the STD LiFE model with discretization parameter $L = 360$.

IV. DISCUSSION

The number of brain dataset collected using modern neuroimaging methods is growing at exponentially fast pace. At the same time both data resolution, as well as the size of the populations of human brains being acquired and shared are growing (Amunts et al, 2013; Scott et al, 2011; Van Essen and Ugurbil, 2012; Van Essen et al, 2013; Zuo et al, 2014). The next generation of brain science will require collaborative efforts between the neuroscience community as well as the informatics and signal processing communities (Garyfallidis et al, 2014; Gorgolewski et al, 2011; Perez and Granger, 2007).

The present article focuses on the application of modern signal processing methods for big data to neuroimaging. More specifically we present an example application to diffusion imaging and tractogra-

phy evaluation (Pestilli et al, 2014). Major value of dMRI and tractography is to allow measuring white-matter in living brains in an individualized manner, one brain at the time. Major efforts are being put forth to improve the representation of the white matter at the macro-, meso- and micro-structural level (Assaf and Basser, 2005; Assaf et al, 2008, 2013; Daducci et al, 2015a,b; Garyfallidis et al, 2012; Pestilli et al, 2014; Smith et al, 2006; Yeatman et al, 2012; Yendiki et al, 2011; Zhang et al, 2012). The digital nature of neuroimaging data and the availability of large in-vivo databases affords developing new methods to built individual connectomes and compute their accuracy, and validate the results (Pestilli et al, 2014).

Computational tractography methods exploit the diffusion-weighted signal measured with MRI to identify plausible trajectories of white matter tracts. Most tractography methods estimate candidate tracts one node at a time. Beyond the great excitement brought about by all these technologies, much work is necessary to develop approaches for evaluation and validation of results (Catani et al, 2012; Jones et al, 2013; Sporns et al, 2005). To date two primary approaches have been used to tractography validation. First, the geometric accuracy of tractography has been compared to simulated and physical phantoms (Fillard et al, 2011; Schreiber et al, 2014; Zheng et al, 2014). Second, tracts and connections identified using tractography have been compared to connections obtained with staining methods in postmortem tissue (Azadbakht et al, 2015; Parker et al, 2002; Seehaus et al, 2013; Sherbondy et al, 2008; Thomas et al, 2014). These validation approaches have helped establishing that tractography is accurate to a certain degree and can well identify tracts within the core white matter.

Attempts to improve tractography have focussed on what is called global tractography. Global tractography methods evaluate the plausibility of the tractography estimates by comparing individual streamlines trajectories with models of the dMRI signal or heuristic rules about streamline smoothness (Aganj et al, 2011; Fillard et al,

2009, 2011; Jbabdi et al, 2007, 2008; Li et al, 2012; Neher et al, 2012; Reisert et al, 2011; Sherbondy et al, 2008). Alternative approaches to global tractography have proposed the concurrent estimation of the biophysical properties of the white matter fascicles and surrounding tissue (Girard et al, 2015; Kaden et al, 2015; Sherbondy et al, 2011, 2009; Zhang and Laidlaw, 2006). Historically global tractography methods have been considered computationally intensive tasks with limited applicability to routine study of the human brain in healthy and diseased populations.

Recently a method for tractography evaluation based on linearized models (Pestilli et al, 2014) has been proposed and applied to study living connectomes (Gomez et al, 2015; Takemura et al, 2015; Yeatman et al, 2014). The method separates the process of tracking from that of global evaluation of the fascicles (Sherbondy et al, 2008). Similarly a family of algorithms based on linearized models have been proposed to solve a series of estimation problems identified in modern tractography, as well as for studying of the tissue microstructure (Daducci et al, 2015a,b). This new generation of linearized methods for microstructure estimation, tractography evaluation are paving the road for new avenues of investigation and the study of the white matter in vivo.

The contribution of the work presented here is to introduce the general framework of multiway decomposition methods that can potentially be applied to any type of linearized neuroimaging models. The decomposition methods allow reducing the computational complexity of the neuroimaging models and in doing so can increase the impact of these models. The application of multiway decomposition methods to neuroimaging will pave the road to use global estimation and evaluation methods to study large populations of human brains with increasingly high spatial resolution and to apply the modern methods to study the human brain in normal and clinical populations such as those available in modern databases (Scott et al, 2011; Van Essen and Ugurbil,

2012; Van Essen et al, 2013).

APPENDIX A: COMPUTATIONAL ALGORITHMS.

Below we report pseudo code for the two operations necessary to fit the decomposed LiFE model. These operations provide the option of being implemented using multi-threading methods. This is because the instances in the loop are independent and allow parallel computations.

Algorithm 1 : $\mathbf{y} = \mathbf{M_times_w}(\Phi, \mathbf{D}, \mathbf{S}_0, \mathbf{w})$

Require: Decomposition components $(\Phi, \mathbf{D}, \mathbf{S}_0)$ and vector $\mathbf{w} \in \mathbb{R}^{N_f}$.

Ensure: $\mathbf{y} = \mathbf{M}\mathbf{w}$

- 1: $\Phi = \Phi \times_2 \mathbf{S}_0$; the result is a very large but still very sparse 3D-array.
 - 2: $\mathbf{Y} = \Phi \times_3 \mathbf{w}^T$; the result is a large but very sparse matrix ($N_a \times N_v$)
 - 3: $\mathbf{Y} = \mathbf{D}\mathbf{Y}$; the result is a relatively small matrix ($N_\theta \times N_v$)
 - 4: $\mathbf{y} = \text{vec}(\mathbf{Y})$
 - 5: **return** \mathbf{y} ;
-

Algorithm 2 : $\mathbf{w} = \mathbf{Mtransp_times_y}(\Phi, \mathbf{D}, \mathbf{S}_0, \mathbf{y})$

Require: Decomposition components $(\Phi, \mathbf{D}, \mathbf{S}_0)$ and vector $\mathbf{y} \in \mathbb{R}^{N_\theta N_v}$.

Ensure: $\mathbf{w} = \mathbf{M}^T \mathbf{y}$

- 1: $\mathbf{Y} \in \mathbb{R}^{N_\theta \times N_v} \leftarrow \mathbf{y} \in \mathbb{R}^{N_\theta N_v}$; reshape vector \mathbf{y} into a matrix \mathbf{Y}
 - 2: $\Phi = \Phi \times_2 \mathbf{S}_0$; the result is a very large but still very sparse 3D-array.
 - 3: $[\mathbf{a}, \mathbf{v}, \mathbf{f}, \mathbf{c}] = \text{get_nonzero_entries}(\Phi)$; $a(n)$, $v(n)$, $f(n)$, $c(n)$ indicate the atom, the voxel, the fascicle and coefficient associated to node n , respectively, with $n = 1, 2, \dots, N_n$;
 - 4: $\mathbf{w} = \mathbf{0} \in \mathbb{R}^{N_f}$; Initialize weights with zeros
 - 5: **for** $n = 1$ to N_n **do**
 - 6: $w(f(n)) = w(f(n)) + \mathbf{D}^T(:, a(n))\mathbf{Y}(:, v(n))c(n)$;
 - 7: **end for**
 - 8: **return** \mathbf{w} ;
-

ACKNOWLEDGEMENTS

We thank Hu Chen, Andrzej Cichocki, Aviv Mezer, Ariel Rokem, Richard Shiffrin, Olaf Sporns and Brian Wandell for comments on early versions of the manuscript. We thank Robert Henschel for support using the high performance computers at Indiana University Bloomington and Holger Brunst for support in C code compilation and performance tuning. This project was funded by Indiana University startup funds to F.P.

REFERENCES

- Aganj I, Lenglet C, Jahanshad N, Yacoub E, Harel N, Thompson PM, Sapiro G (2011) A Hough transform global probabilistic approach to multiple-subject diffusion MRI tractography. *Medical Image Analysis* 15(4):414–425
- Amunts K, Lepage C, Borgeat L, Mohlberg H, Dickscheid T, Rousseau ME, Bludau S, Bazin PL, Lewis LB, Oros-Peusquens AM, Shah NJ, Lippert T, Zilles K, Evans AC (2013) BigBrain: an ultrahigh-resolution 3D human brain model. *Science* 340(6139):1472–1475
- Assaf Y, Basser PJ (2005) Composite hindered and restricted model of diffusion (CHARMED) MR imaging of the human brain. *NeuroImage* 27(1):48–58
- Assaf Y, Blumenfeld-Katzir T, Yovel Y, Basser PJ (2008) Axcaliber: A method for measuring axon diameter distribution from diffusion MRI. *Magnetic Resonance in Medicine* 59(6):1347–1354
- Assaf Y, Alexander DC, Jones DK, Bizzi A, Behrens TEJ, Clark CA, Cohen Y, Dyrby TB, Huppi PS, Knoesche TR, LeBihan D, Parker GJM, Poupon C, consortium C (2013) The CONNECT project: Combining macro- and micro-structure. *NeuroImage* 80(C):273–282
- Azadbakht H, Parkes LM, Haroon HA, Augath M, Logothetis NK, de Crespigny A, D’Arceuil HE, Parker GJM (2015) Validation of high-resolution tractography against In vivo tracing in the macaque visual cortex. *Cerebral Cortex*
- Bader BW, Kolda TG, others (2012) MATLAB Tensor Toolbox Version 2.5. Tech. rep., Sandia National Laboratories
- Basser P, Mattiello J, LeBihan D (1994) Estimation of the effective self-diffusion tensor from the NMR spin echo. *Journal of Magnetic Resonance, Series B* 103(3):247–254
- Basser PJ, Pierpaoli C (2011) Microstructural and physiological features of tissues elucidated by quantitative-diffusion-tensor MRI. *Journal of Magnetic Resonance* 213(2):560–570
- Basser PJ, Pajevic S, Pierpaoli C, Duda J, Aldroubi A (2000) In vivo fiber tractography using DT-MRI data. *Magnetic Resonance in Medicine* 44(4):625–632
- Behrens T, Johansen-Berg H, Woolrich M, Smith S, Wheeler-Kingshott C, Boulby P, Barker G, Sillery E, Sheehan K, Ciccarelli O (2003a) Non-invasive mapping of connections between human thalamus and cortex using diffusion imaging. *Nature Neuroscience* 6(7):750–757
- Behrens TEJ, Woolrich MW, Jenkinson M, Johansen-Berg H, Nunes RG, Clare S, Matthews PM, Brady JM, Smith SM (2003b) Characterization and propagation of uncertainty in diffusion-weighted MR imaging. *Magnetic Resonance in Medicine* 50(5):1077–1088
- Caiafa CF, Cichocki A (2012) Computing Sparse representations of multidimensional signals using Kronecker bases. *Neural Computation* pp 186–220
- Caiafa CF, Cichocki A (2013) Multidimensional compressed sensing and their applications. *Wiley Interdisciplinary Reviews: Data Mining and Knowledge Discovery* 3(6):355–380
- Catani M, Bodi I, Dell’Acqua F (2012) Comment on “The geometric structure of the brain fiber pathways”. *Science* 337(6102):1605–1605
- Cichocki A, Mandic D, De Lathauwer L, Zhou G, Zhao Q, Caiafa C, Phan AH (2015) Tensor decompositions for signal processing applications: from two-way to multiway component analysis. *IEEE signal processing magazine* 32:145–163
- Cook P, Bai Y, Nedjati-Gilani S, Seunarine KK, Hall MG, Parker GJ, Alexander DC (2006) Camino: open-source diffusion-MRI reconstruction and processing. In: 14th Scientific Meeting of the International Society for Magnetic Resonance in Medicine, Seattle
- Daducci A, Canales-Rodríguez EJ, Zhang H, Dyrby TB, Alexander DC, Thiran JP (2015a) Accelerated Microstructure Imaging via Convex Optimization (AMICO) from diffusion MRI data. *NeuroImage* 105(C):32–44
- Daducci A, Palù AD, Lemkaddem A, Thiran JP (2015b) COMMIT: Convex optimization modeling for microstructure informed tractography. *Medical Imaging, IEEE Transactions on* 34(1):246–257
- Fillard P, Poupon C, Mangin JF (2009) A novel global tractography algorithm based on an adaptive spin glass model. *Audio, Transactions of the IRE Professional Group on* 12(Pt 1):927–934
- Fillard P, Descoteaux M, Goh A, Gouttard S, Jeurissen B, Malcolm J, Ramirez-Manzanares A, Reisert M, Sakaie K, Tensaouti F, Yo T, Mangin JF, Poupon C (2011) Quantitative evaluation of 10 tractography algorithms on a realistic diffusion MR phantom. *NeuroImage* 56(1):220–234
- Fischl B (2012) FreeSurfer. *NeuroImage* 62(2):774–781
- Frank LR (2002) Characterization of anisotropy in high angular resolution diffusion-weighted MRI. *Magnetic Resonance in Medicine* 47(6):1083–1099
- Friston KJ, Ashburner J, Frith CD, Poline JB, Heather JD, Frackowiak RSJ (2004) Spatial registration and normalization of images. *Human Brain Mapping* 3(3):165–189

- Garyfallidis E, Brett M, Correia MM, Williams GB, Nimmo-Smith I (2012) QuickBundles, a method for tractography simplification. *Frontiers in Neuroscience* 6:175–175
- Garyfallidis E, Brett M, Amirbekian B, Rokem A, van der Walt S, Descoteaux M, Nimmo-Smith I, Nimmo-Smith I (2014) Dipy, a library for the analysis of diffusion MRI data. *Frontiers in Neuroinformatics* 8:8–8
- Girard G, Fick R, Descoteaux M, Deriche R (2015) AxTract: microstructure-driven tractography based on the ensemble average propagator. In: *Information Processing in Medical Imaging*, Isle of Skye
- Gomez J, Pestilli F, Witthoft N, Golarai G, Liberman A, Poltoratski S, Yoon J, Grill-Spector K (2015) Functionally defined white matter reveals segregated pathways in human ventral temporal cortex associated with category-specific processing. *Neuron* 85(1):216–227
- Gorgolewski K, Burns CD, Madison C, Clark D, Halchenko YO, Waskom ML, Ghosh SS (2011) Nipype: a flexible, lightweight and extensible neuroimaging data processing framework in Python. *Frontiers in Neuroinformatics* 5:13–13
- Jbabdi S, Woolrich MW, Andersson JLR, Behrens TEJ (2007) A Bayesian framework for global tractography. *Human Brain Mapping Journal* 37(1):116–129
- Jbabdi S, Bellec P, Toro R, Daunizeau J, Péligrini-Issac M, Benali H (2008) Accurate anisotropic fast marching for diffusion-based geodesic tractography. *International Journal of Biomedical Imaging* 2008(1-2):1–12
- Jiang H, van Zijl PCM, Kim J, Pearlson GD, Mori S (2006) DtiStudio: Resource program for diffusion tensor computation and fiber bundle tracking. *Computer Methods and Programs in Biomedicine* 81(2):106–116
- Jones DK, Horsfield MA, Simmons A (1999) Optimal strategies for measuring diffusion in anisotropic systems by magnetic resonance imaging. *Magnetic Resonance in Medicine* 42(3):515–525
- Jones DK, Knösche TR, Turner R (2013) White matter integrity, fiber count, and other fallacies: the do's and don'ts of diffusion MRI. *NeuroImage* 73:239–254
- Kaden E, Kruggel F, Alexander DC (2015) Quantitative mapping of the per-axon diffusion coefficients in brain white matter. *Magnetic Resonance in Medicine*
- Kim D, Sra S, Dhillon IS (2013) A non-monotonic method for large-scale non-negative least squares. *Optimization Methods and Software* 28(5):1012–1039
- Kolda T, Bader B (2009) Tensor decompositions and applications. *SIAM Review* 51(3):455–500
- Lazar M, Weinstein DM, Tsuruda JS, Hasan KM, Arfanakis K, Meyerand ME, Badie B, Rowley HA, Houghton V, Field A, Alexander AL (2003) White matter tractography using diffusion tensor deflection. *Human Brain Mapping* 18(4):306–321
- Li L, Rilling JK, Preuss TM, Glasser MF, Damen FW, Hu X (2012) Quantitative assessment of a framework for creating anatomical brain networks via global tractography. *Human Brain Mapping Journal* 61(4):1017–1030
- Mørup M (2011) Applications of tensor (multiway array) factorizations and decompositions in data mining. *Wiley Interdisciplinary Reviews: Data Mining and Knowledge Discovery* 1(1):24–40
- Neher PF, Stieltjes B, Reisert M, Reicht I, Meinzer HP, Fritzsche KH (2012) Medical imaging 2012: image Processing. In: Haynor DR, Ourselin S (eds) *SPIE Medical Imaging*, SPIE, p 83144D
- Parker GJM, Stephan KE, Barker GJ, Rowe JB, MacManus DG, Wheeler-Kingshott CAM, Ciccarelli O, Passingham RE, Spinks RL, Lemon RN (2002) Initial demonstration of in vivo tracing of axonal projections in the macaque brain and comparison with the human brain using diffusion tensor imaging and fast marching tractography. *NeuroImage* 15(4):797–809
- Parker GJM, Haroon HA, Wheeler-Kingshott CAM (2003) A framework for a streamline-based Probabilistic Index of Connectivity (PICO) using a structural interpretation of MRI diffusion measurements. *Journal of Magnetic Resonance Imaging* 18(2):242–254
- Perez F, Granger B (2007) IPython: A system for interactive scientific computing. *Computing in Science & Engineering* 9(3):21–29
- Pestilli F (2015) Test-retest measurements and digital validation for in vivo neuroscience. *Scientific Data* 2:140,057
- Pestilli F, Yeatman JD, Rokem A, Kay KN, Wandell BA (2014) Evaluation and statistical inference for human connectomes. *Nature Methods* 11(10):1058–1063
- Reisert M, Mader I, Anastasopoulos C, Weigel M, Schnell S, Kiselev V (2011) Global fiber reconstruction becomes practical. *Human Brain Mapping Journal* 54(2):955–962
- Rokem A, Yeatman JD, Pestilli F, Kay KN, Mezer A, van der Walt S, Wandell BA (2015) Evaluating the accuracy of diffusion MRI models in white matter. *PLoS ONE* 10(4):e0123,272
- Samanez-Larkin GR, Knutson B (2015) Decision making in the ageing brain: changes in affect

- tive and motivational circuits. *Nature Reviews: Neuroscience* pp 1–13
- Schreiber J, Riffert T, Anwander A, Knösche TR (2014) Plausibility Tracking: A method to evaluate anatomical connectivity and microstructural properties along fiber pathways. *NeuroImage* 90(C):163–178
- Scott A, Courtney W, Wood D, de la Garza R, Lane S, King M, Wang R, Roberts J, Turner JA, Calhoun VD (2011) COINS: An innovative informatics and neuroimaging tool suite built for large heterogeneous datasets. *Frontiers in Neuroinformatics* 5:33–33
- Seehaus AK, Roebroek A, Chiry O, Kim DS, Ronen I, Bratzke H, Goebel R, Galuske RAW (2013) Histological validation of DW-MRI tractography in human postmortem tissue. *Cerebral Cortex* 23(2):442–450
- Sherbondy A, Dyrby T, Rowe M, Ptito M (2011) Microstructure tracking (Microtrack): an algorithm for estimating a multiscale hierarchical white matter model from diffusion-weighted MRI. In: *Proceedings of the 19th International Society for Magnetic Resonance in Medicine, Montreal*
- Sherbondy AJ, Dougherty RF, Ben-Shachar M, Napel S, Wandell BA (2008) ConTrack: Finding the most likely pathways between brain regions using diffusion tractography. *Journal of Vision* 8(9):15–15
- Sherbondy AJ, Dougherty RF, Ananthanarayanan R, Modha DS, Wandell BA (2009) Think global, act local; projectome estimation with BlueMatter. *Audio, Transactions of the IRE Professional Group on 12(Pt 1):861–868*
- Smith SM, Jenkinson M, Johansen-Berg H, Rueckert D, Nichols TE, Mackay CE, Watkins KE, Ciccarelli O, Cader MZ, Matthews PM, Behrens TEJ (2006) Tract-based spatial statistics: Voxelwise analysis of multi-subject diffusion data. *NeuroImage* 31(4):1487–1505
- Sporns O, Tononi G, Kötter R (2005) The human connectome: A structural description of the human brain. *PLoS Computational Biology* 1(4):e42–e42
- Stejskal EO, Tanner JE (1965) Spin Diffusion Measurements: Spin Echoes in the Presence of a Time-Dependent Field Gradient. *The Journal of Chemical Physics* 42(1):288
- Takemura H, Rokem A, Winawer J, Yeatman JD, Wandell BA, Pestilli F (2015) A major human white matter pathway between dorsal and ventral visual cortex. *Cerebral Cortex*
- Thomas C, Ye FQ, Irfanoglu MO, Modi P, Saleem KS, Leopold DA, Pierpaoli C (2014) Anatomical accuracy of brain connections derived from diffusion MRI tractography is inherently limited. *Proceedings of the National Academy of Sciences* 111(46):16,574–16,579
- Thomason ME, Thompson PM (2011) Diffusion imaging, white matter, and psychopathology. *Clinical Psychology* 7:63–85
- Tournier JD, Calamante F, Connelly A (2012) MRtrix: Diffusion tractography in crossing fiber regions. *International Journal of Imaging Systems and Technology* 22(1):53–66
- Tucker LR (1966) Some mathematical notes on three-mode factor analysis. *Psychometrika* 31(3):279–311
- Van Essen DC, Ugurbil K (2012) The future of the human connectome. *NeuroImage* 62(2):1299–1310
- Van Essen DC, Smith SM, Barch DM, Behrens TEJ, Yacoub E, Ugurbil K, Consortium ftWMH (2013) The WU-Minn Human Connectome Project: An overview. *NeuroImage* 80(C):62–79
- Yeatman JD, Dougherty RF, Myall NJ, Wandell BA, Feldman HM (2012) Tract profiles of white matter properties: automating fiber-tract quantification. *PLoS ONE* 7(11):e49,790
- Yeatman JD, Weiner KS, Pestilli F, Rokem A, Mezer A, Wandell BA (2014) The vertical occipital fasciculus: A century of controversy resolved by in vivo measurements. *Proceedings of the National Academy of Sciences* 111(48):E5214–E5223
- Yendiki A, Panneck P, Srinivasan P, Stevens A, Zöllei L, Augustinack J, Wang R, Salat D, Ehrlich S, Behrens T, Jbabdi S, Gollub R, Fischl B (2011) Automated probabilistic reconstruction of white-matter pathways in health and disease using an atlas of the underlying anatomy. *Frontiers in Neuroinformatics* 5:23–23
- Zhang H, Schneider T, Wheeler-Kingshott CA, Alexander DC (2012) NODDI: Practical in vivo neurite orientation dispersion and density imaging of the human brain. *NeuroImage* 61(4):1000–1016
- Zhang S, Laidlaw DH (2006) Sampling DTI fibers in the human brain based on DWI forward modeling. *International Conference of the IEEE Engineering in Medicine and Biology Society Proceedings* 1:4885–4888
- Zhang Y, Zhang J, Oishi K, Faria AV, Jiang H, Li X, Akhter K, Rosa-Neto P, Pike GB, Evans A, Toga AW, Woods R, Mazziotta JC, Miller MI, van Zijl PCM, Mori S (2010) Atlas-guided tract reconstruction for automated and comprehensive examination of the white matter anatomy. *NeuroImage* 52(4):1289–1301
- Zheng C, Pestilli F, Rokem A (2014) Quantifying error in estimates of human brain fiber direc-

tions using Earth Mover's Distance. arXivorg
stat.ML:5271

Zuo XN, Anderson JS, Bellec P, Birn RM, Biswal
BB, Blautzik J, Breitner JCS, Buckner RL, Cal-
houn VD, Castellanos FX, Chen A, Chen B,
Chen J, Chen X, Colcombe SJ, Courtney W,
Craddock RC, Di Martino A, Dong HM, Fu X,
Gong Q, Gorgolewski KJ, Han Y, He Y, He Y,
Ho E, Holmes A, Hou XH, Huckins J, Jiang T,
Jiang Y, Kelley W, Kelly C, King M, LaConte
SM, Lainhart JE, Lei X, Li HJ, Li K, Li K, Lin
Q, Liu D, Liu J, Liu X, Liu Y, Lu G, Lu J, Luna

B, Luo J, Lurie D, Mao Y, Margulies DS, Mayer
AR, Meindl T, Meyerand ME, Nan W, Nielsen
JA, O'Connor D, Paulsen D, Prabhakaran V, Qi
Z, Qiu J, Shao C, Shehzad Z, Tang W, Villringer
A, Wang H, Wang K, Wei D, Wei GX, Weng XC,
Wu X, Xu T, Yang N, Yang Z, Zang YF, Zhang
L, Zhang Q, Zhang Z, Zhang Z, Zhao K, Zhen
Z, Zhou Y, Zhu XT, Milham MP (2014) An open
science resource for establishing reliability and
reproducibility in functional connectomics. Sci-
entific Data 1:140,049